



Efficient hollow cubic Co₉S₈@defective ZnS/g-C₃N₄ for multi-pollutants removal via cascade Z-scheme heterojunction

Chengyuan Yang^a, Jing Wang^a, Rong Wang^a, Wenxin Zhu^a, Liang Zhang^a, Ting Du^a,
Jing Sun^b, Ming-Qiang Zhu^c, Yizhong Shen^{d,*}, Jianlong Wang^{a,*}

^a College of Food Science and Engineering, Northwest A&F University, Yangling 712100, Shaanxi, China

^b Qinghai Provincial Key Laboratory of Qinghai-Tibet Plateau Biological Resources, Northwest Institute of Plateau Biology, Chinese Academy of Sciences, Qinghai 810008, China

^c College of Mechanical and Electronic Engineering, Northwest A&F University, Yangling 712100, China

^d School of Food and Biological Engineering, Hefei University of Technology, Hefei 230009, China

ARTICLE INFO

Keywords:

Cascade Z-scheme heterojunction
Defect interface
Hollow cubic structure
Ciprofloxacin
Chromium

ABSTRACT

Multi-pollutants environment coexisted organic and inorganic pollutants has become a common phenomenon, seriously affecting water biodiversity and human water security. Currently, the removal of organic and inorganic pollutants by photocatalysis are mostly in own single-pollutant environment, not in multi-pollutants system, where the common photocatalysts cannot achieve efficiently charge separate and transfer with low reactive oxygen species (ROS) efficiency. Herein, we constructed an efficient cascaded Z-scheme heterojunction Co₉S₈@defective ZnS/g-C₃N₄ (C@DZ/N) composed of defective engineering in hollow nanocubes, which achieved excellent photodegradation activity (98.93 % for ciprofloxacin (CIP) and 97.18 % for Cr(VI) at 90 min) in multi-pollutants environment, significantly higher than the hollow cubic with Z-scheme heterojunction in single-pollutant environment (98.07 % for CIP and 98.72 % for Cr(VI) at 140 min). Defective ZnS acts as the core for direct charge transfer and separation to form a unique cascaded Z-scheme heterojunction system that blocks the type II charge transfer pathway to achieve ultra-efficient charge transfer. Furthermore, the structural characterization and ROS experimental results based on multi-pollutants models show that the cascade Z-scheme system greatly facilitates the ROS release kinetics and further leads to more electron-deficient cubic surfaces while increase the directional conversion to singlet oxygen (¹O₂) in multi-pollutants environment. Further tests of intermediates and reusability indicated its potential for the high-efficient treatment of multiple pollution systems.

1. Introduction

Multi-pollutants environment coexisted organic and inorganic pollutants seriously affect water biodiversity and human water security [1–5]. Simultaneous multi-pollutants removal has important implications on environment remediation, since both are highly persistent, bio-accumulative, and non-biodegradable [6–8]. Photocatalysis as an advanced oxidation process (AOP), which is a sustainable solar energy harvesting, and environmentally friendly photo-oxidation processes, has shown its promising application in the degradation of various stubborn pollutants [9–14]. However, the removal of organics and heavy metals by photocatalysis are mostly based on dispersed treatment, not in multi-pollutants system, which could be attributed to the inflexible

charge separate and transfer in photocatalysts and subsequently result in low ROS generation, as well as the mutually exclusive requirements of photodegradation and photoreduction [10,15–17]. Moreover, ROS efficiency for the removal of multiple pollutants is still limited due to the competitive of anisotropic reaction [18,19]. Thus, it is still a big challenge for an ideal photocatalyst design on enhancing the efficiency of ROS in multi-pollutants remediation.

Constructing hollow cubic engineering system is an effective way to achieve efficient electron-hole pairs and ROS generation, which retains both advantages of cube and hollow structures, including efficient solar energy collection as well as the exposed more sides and facets [20,21]. Among a series of hollow cubic crystals (such as Zn₂SnO₄, Cu_{2-x}S, CdS, MoS₂), Co₉S₈ is widely reported because of its simple preparation

* Corresponding authors.

E-mail addresses: yzshen@hfut.edu.cn (Y. Shen), wanglong79@nwsuaf.edu.cn (J. Wang).

<https://doi.org/10.1016/j.apcatb.2022.122084>

Received 27 July 2022; Received in revised form 24 September 2022; Accepted 17 October 2022

Available online 18 October 2022

0926-3373/© 2022 Elsevier B.V. All rights reserved.

method. However, the hollow structure is relatively weak in photocatalytic process, and mass transfer to disable the active sites on the inner surface may be restricted [22–24]. One promising strategy could be achieved by construction hierarchically hollow structures in multi-shell or yolk-shell architectures, which exhibit good structural stability by mutual supporting effect. However, this strategy required for the complicated synthesis process and still limited in internal voids transport [20,25,26]. Specifically, constructing Z-scheme heterojunctions by coupling materials with different energy level structures could improve the photocatalytic performance of hollow cubic system, which was achieved by fast separation and migration of photogenerated electrons and holes [27–29]. For the Z-scheme heterojunction, it requires for matching the bandgap structure where the conduction band of one semiconductor should be as close as possible to the valence band of the others. The perplex is that what happen to electrons transferring through Z-scheme heterojunction also accompanied with conventional type II heterojunction, which means the charge transfer pathways sacrificed the redox potentials of the photogenerated charge carriers [30,31]. Therefore, designing a cascaded Z-scheme system while introducing interfacial defects as the core of the direct charge transfer and separation, may block the type II charge transfer pathway [30,32]. In addition, interfacial defects also serve as anchor sites for other semiconductors, connecting with chemical bonds act as specific "bridges" to form unique heterojunction interfaces for accelerate charge transfer between semiconductors [33,34]. Benefiting from this unique structure, it provides an ideal theoretical and experimental model for its enhanced ROS generation efficiency in multi-pollutants environments. However, the indiscriminate decomposition of contaminants caused by ROS is less desirable and even goes against their final degradation somehow, which may be transformed to other high toxic organics as intermediate and generate final products without complete degradation [35,36]. Furthermore, the deliberately regulation of excellent oxidant generation to improve ROS utilization efficiency also requires further investigation in multi-pollutants environment.

The defective ZnS has been chosen for the "bridges" of electron transfer as it has the modified original electronic structure and connected the semiconductors in anchored relationship, which coupled Co_9S_8 and $\text{g-C}_3\text{N}_4$ to realize the cascade Z-scheme heterojunction that minimize the charge recombination and exhibit exceptional activities for both photodegradation and photoreduction. With that, we construct a unique cascade Z-scheme system named C@DZ/N in hollow cubic photocatalyst, where a defective engineering was introduced to modulate the Z-Scheme heterojunction for efficient multi-pollutants remediation. The common refractory organic pollutants CIP and Cr(VI) were selected as organic and inorganic model pollutants. Structure characteristic and photocatalytic properties of C@DZ/N were investigated. The promoting degradation mechanisms in multi-pollutants environments were demonstrated. Experimental results confirmed that the cascade Z-scheme system formed by defective ZnS accelerate the electron transfer by improving the direct Z-scheme efficiency, further promoted the ROS reaction efficiently on the surface of hollow cubic C@DZ/N. This work not only demonstrates that the cascade Z-scheme heterojunctions with defect engineering promote charge separation and transfer, but also provide efficient photocatalytic reactions for multi-pollutants removal.

2. Materials and methods

2.1. Materials

Cobalt nitrate hexahydrate ($\text{Co}(\text{NO}_3)_2 \cdot 6\text{H}_2\text{O}$), zinc nitrate hexahydrate ($\text{Zn}(\text{NO}_3)_2 \cdot 6\text{H}_2\text{O}$), 2-methylimidazole, hexadecyl trimethyl ammonium bromide (CTAB), thioacetamide (TAA), thiourea ($\text{CN}_2\text{H}_4\text{S}$), are all analytically grade and purchased from Aladdin Chemical Co., Ltd.

2.2. Synthesis of materials

2.2.1. Synthesis of CoS_x

In a typical synthesis, 40 mg of the ZIF-67 was added into 20 mL of an ethanol solution containing 50 mg of TAA, and ultrasound for 2 min. Then, the resulting mixture was transferred to a Teflon-lined autoclave (50 mL capacity) and kept at 180 °C for 3 h in oven. After cooling to room temperature, the precipitate was washed six times with ethanol.

2.2.2. Synthesis of $\text{CoS}_x/\text{ZIF-8}$

295.2 mg of 2-methylimidazole was dissolved in 30 mL of ethanol and stirred for 10 min in ice bath. 20 mg of CoS_x was added to the solution and then stirred for another 30 min. Subsequently, 99.2 mg of $\text{Zn}(\text{NO}_3)_2 \cdot 6\text{H}_2\text{O}$ was dissolved in 20 mL of ethanol and then slowly added to the above solution, then continuously stirred in 1 h.

2.2.3. Synthesis of C@DZ/N

200 mg of $\text{CoS}_x/\text{ZIF-8}$, 200 mg thiourea and 100 mg $\text{g-C}_3\text{N}_4$ were added to a crucible boat and heated at 550 °C for 6 h in argon atmosphere at a heating rate of 5 °C/min. Co_9S_8 , $\text{Co}_9\text{S}_8/\text{g-C}_3\text{N}_4$ and $\text{Co}_9\text{S}_8/\text{defective ZnS}$ were obtained by same thermal treatment.

2.3. Characterization

X-ray diffraction (XRD) was employed to examine crystal structure of materials (D8 advance, Bruker, Japan). Fourier transform infrared (FT-IR) spectrum was achieved with a spectrometer at 18–25 °C (Nicolet-6700, Thermo, USA). X-ray photoelectron spectroscopy (XPS) patterns were conducted on a spectrometer (Escalab 250Xi, Thermo Scientific, USA). A field emission scanning electron microscope (Hitachi S-4800, Japan) was used to observe the morphology. Transmission electron microscopy (TEM) and selected area electron diffraction (SAED) images were collected on a JEM-1230 to determine the morphological features. Diffuse reflectance spectra (DRS) were acquired by a UV-vis spectrometer (UV-2600, Shimadzu, Japan). Photoluminescence (PL) was done through a fluorescence spectrophotometer (HoribaHR500, USA) at 370 nm. The irradiation power used for photocatalytic reactions and PEC experiments was 400 mW/cm² and $\lambda > 420$ nm in Xe lamp irradiation.

2.4. Photocatalytic degradation and reduction test

The properties of C@DZ/N were examined through degrading refractory antibiotic ciprofloxacin. Experimental procedures are as follows: 0.010 g catalyst was dissolved into a beaker containing a 100 mL CIP solution (10 mg/L), 100 mL Cr(VI) solution (20 mg/L), 100 mL mixed solution and experienced ultrasonic treatment for a few minutes to form homogeneous mixture, respectively. Subsequently, the mixtures were continuously stirred in the dark for 40 min to reach adsorption equilibrium. After that, the mixture began to undergo irradiation from Xenon lamp (300 W). Finally, the degraded product was determined by UV-vis Spectrophotometer at room temperature.

2.5. Photoelectrochemical test

The photo-electrochemical performance of C@DZ/N was analyzed via an electro-chemical workstation (CHI660E, ChenHua, China) with platinum wires, Ag/AgCl and sodium sulfate solution (0.5 mol/L) as reverse electrode, reference electrode and electrolyte solution, respectively. Transient photocurrent spectra (TPR) were examined with a voltage 0.5 V and 20 s intervals.

2.6. Active species trapping experiments

1.0 mmol/L 1,4-benzoquinone (BQ), 1.0 mmol/L LAA, 1.0 mmol/L TEMP and 1.0 mmol/L TBA were applied for superoxide radical ($\cdot\text{O}_2^-$), electron (e^-), single oxygen ($^1\text{O}_2$) and hydroxyl radical ($\cdot\text{OH}$),

respectively. Moreover, electron spin resonance (ESR) experiment used 5,5-dimethyl-1-pyrroline-N-oxide (DMPO) as scavengers to determine $\cdot\text{OH}$, $^1\text{O}_2$ and $\cdot\text{O}_2$ radicals.

3. Results and discussion

3.1. Fabrication and characterization of ternary heterogeneous C@DZ/N

Describing the whole synthesis process in detail (Fig. 1a-g), hollow CoS_x was prepared by hydrothermal method with ZIF-67 as the precursor, and the final C@DZ/N was formed by calcination with the introduction of ZIF-8 and g- C_3N_4 . The morphology and detailed structure of the as-prepared Co_9S_8 , Co_9S_8 @defective ZnS and C@DZ/N were characterized. As shown in Fig. S1, the morphology of C@DZ/N retain the nanocubic structure, where the defective ZnS and g- C_3N_4 were intimately form close contact on the surface of Co_9S_8 . However, compared to the hollow cubic structure of Co_9S_8 and Co_9S_8 @defective ZnS, the size of C@DZ/N is dramatically expanded, which ascribed to the uniformly anchored of the ultrathin g- C_3N_4 nanosheets. The HRTEM images in Fig. 1h and i clearly show the intimate ternary heterogeneous interface of C@DZ/N, in which the detailed lattice planes are consistent with the Co_9S_8 and ZnS signed in detail. In addition, the lattice fringes in the outer edge of ZnS became less ordered and unidentified, which indicate the existence of interface defects. The view of EELS element mapping in Fig. 1j reveals the well distribution of Co, Zn and S on the hollow nanocage including Co_9S_8 and the defective ZnS, and the surface of C@DZ/N are all covered with the element of C and N ascribed to the

component of g- C_3N_4 .

Detailed crystalline structure of Co_9S_8 , Co_9S_8 @ZnS, Co_9S_8 @defective ZnS and C@DZ/N were characterized by XRD. As shown in Fig. 2a, the XRD spectrum of C@DZ/N matched Co_9S_8 (JCPDS No. 86-2273), pure zinc blende (cubic) ZnS (JCPDS No.05-0566), and g- C_3N_4 (JCPDS No. 87-1526) (Fig. S2), reconfirming the successful synthesis of C@DZ/N composite [10,37]. Particularly, the characteristic diffraction peaks of ZnS showed a slight shift of 2θ value in Fig. 2b, indicating the deformation of crystal lattices were caused by the significantly contracted vacancies due to the defects of non-stoichiometric precursor feed [38]. In this way, it can be proved that abundant vacancies are expected in the heterogeneous C@DZ/N. These results provide preliminary evidence for the successful preparation of the ternary hollow nanocube with defect engineering.

To further evaluate the functionalization of defective ZnS and g- C_3N_4 on the surface of Co_9S_8 , the FTIR and XPS characterization of each component were obtained. As shown in Fig. 2c, the FTIR spectrum of C@DZ/N displayed the characteristic peaks of Co-S (618 cm^{-1}) and breathing model triazine unit (807 cm^{-1}) in the functional groups of Co_9S_8 @defective ZnS, and g- C_3N_4 , respectively [39]. Subsequently, the N spectrum of XPS showed typical groups of the triazine ring (C=N-C), tertiary N and C-N-H at 396.74, 397.37 and 398.13 eV, representing the introduction of g- C_3N_4 , while the signal of C 1s shifted to the higher binding energies (Fig. S3) [6,10]. Moreover, the surface composition of Co_9S_8 and defective ZnS of C@DZ/N were further demonstrated by XPS. As shown in Fig. 2d, a new set of weak peaks in S 2p spectrum at 162.16 and 164.28 eV indicate the presence of sulfur vacancies. Meanwhile, the

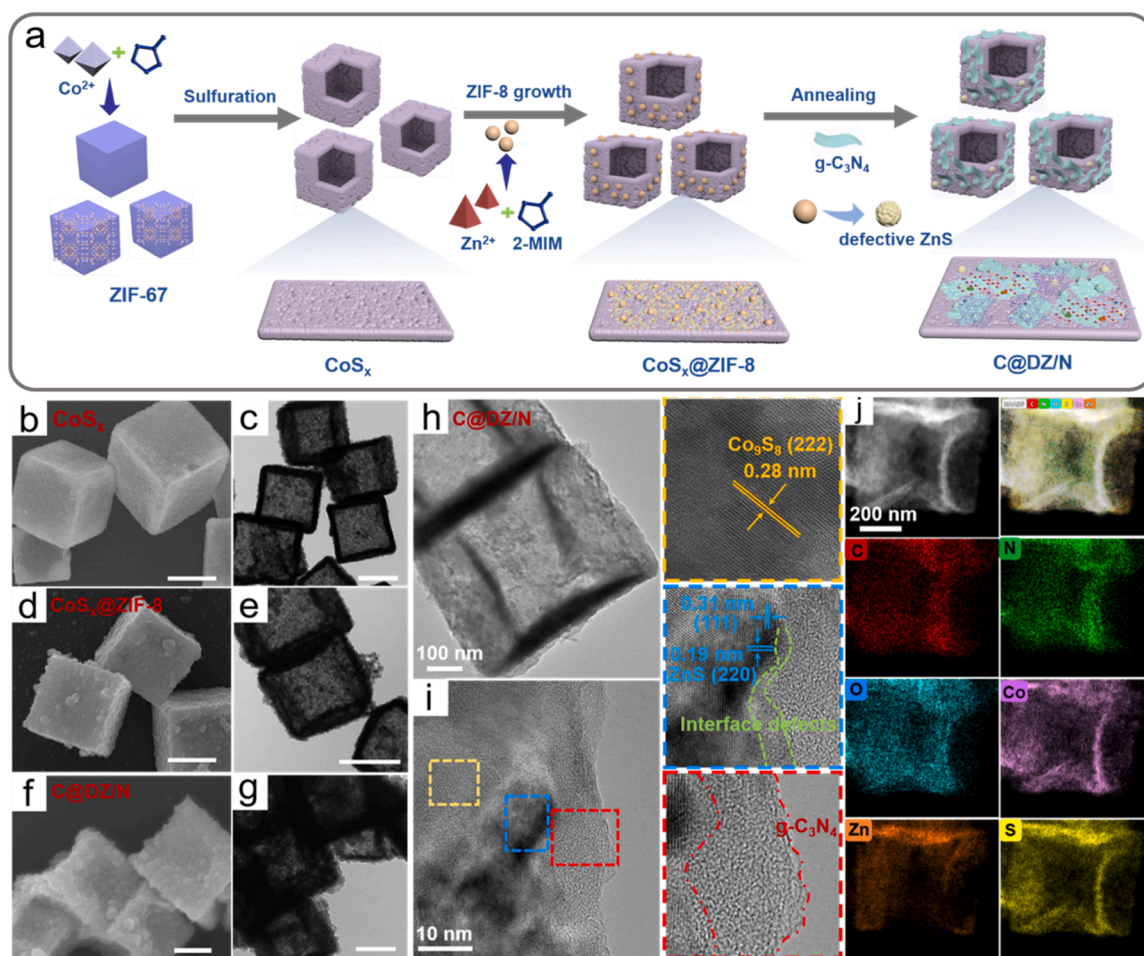


Fig. 1. Schematic illustration the synthetic strategy and morphology characterization. (a) Schematic illustration of the preparation process of C@DZ/N; SEM and TEM images of (b, c) CoS_x , (d, e) CoS_x @ZIF-8, (f, g) C@DZ/N, the scale bars correspond to 300 nm; (h, i) HRTEM images of C@DZ/N; (j) HAADF-STEM images and EDS element mappings.

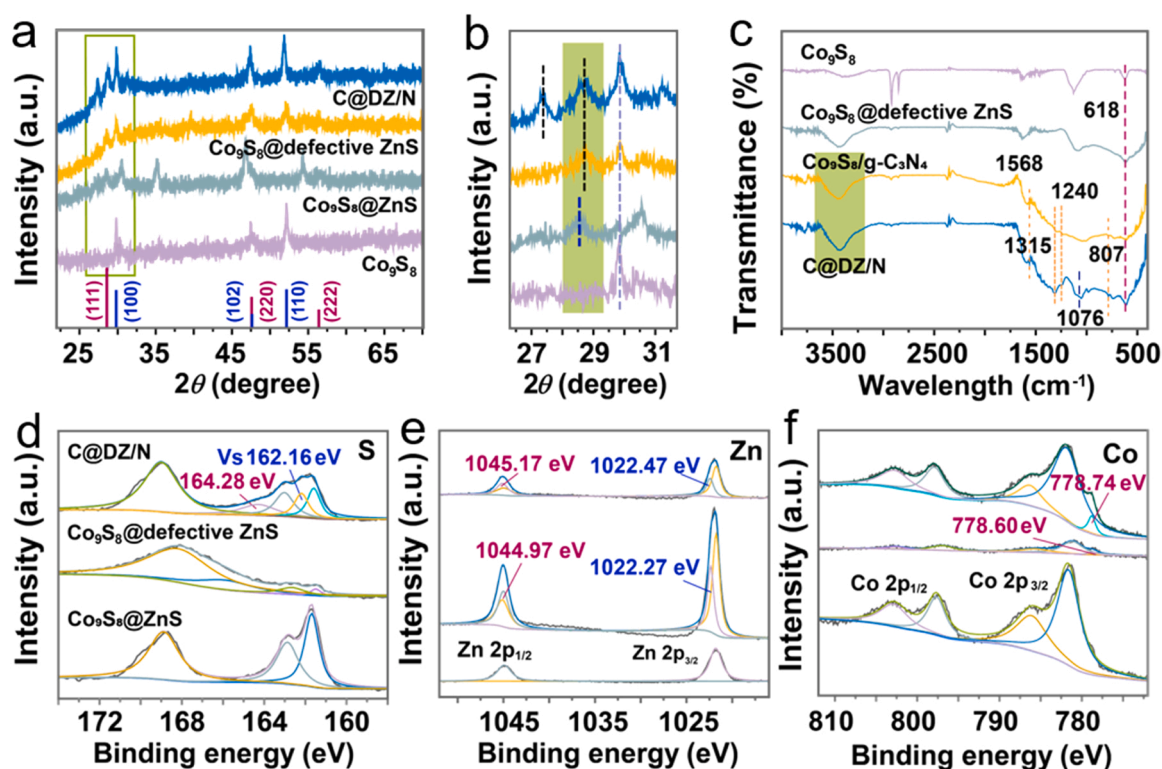


Fig. 2. Composition characterizations of ternary heterogeneous C@DZ/N. (a) XRD patterns of Co₉S₈, Co₉S₈@ZnS, Co₉S₈@defective ZnS and C@DZ/N (ZnS: JCPDS No. 05-0566 in red); Co₉S₈: JCPDS No. 86-2273 in blue); (b) Magnification of panel (a) at the range of 26.3–31.7°; (c) FTIR spectra of Co₉S₈, Co₉S₈@defective ZnS, Co₉S₈/g-C₃N₄ and C@DZ/N; XPS spectra of (d) S 2p, (e) Zn 2p, (f) Co 2p for C@DZ/N, Co₉S₈@defective ZnS, Co₉S₈@ZnS.

peaks of S at 161.62 and 163.02 eV were attributed to the S 2p_{3/2} and S 2p_{1/2} core levels, which shifted to higher binding energies after the introduction of defective ZnS. It is inferred that the positively charged sulfur vacancies in defective ZnS significantly reduce the overall electron density, thereby enhancing the binding energy of the surrounding sulfur species to form a unique heterojunction contact interface [33,38]. In Fig. 2e, the peaks of Zn at 1022.17 and 1044.86 eV were ascribed to the original lattice Zn site. With the appearance of sulfur vacancy density, the binding energies of Zn adjacent to the vacancy in Co₉S₈@defective ZnS were found at 1022.27 and 1044.97 eV. Moreover, the peaks of C@DZ/N at 1022.47 and 1045.17 eV represented the binding energies of Zn adjacent to the vacancies, which were shifted to a higher level compared to Co₉S₈@defective ZnS, indicating the defect-rich characteristic of C@DZ/N [38,40]. Furthermore, the binding energies of Zn 2p_{1/2} and Zn 2p_{3/2} were found shifting to a higher level in Co₉S₈@defective ZnS and C@DZ/N, which results from the electron transition through the interface and the introduction of Zn-rich defect states due to little asymmetry after sulfidation treatment [41,42]. As summarized in Fig. S4 and Table S1, the relative integrate intensity of defect related Zn 2p peak areas associated with the defect increase, which was calculated to 43.7 % and 45.2 % for Zn 2p_{1/2} and 35.2 % and 38.3 % for Zn 2p_{3/2} in Co₉S₈@defective ZnS and C@DZ/N samples, respectively. The relative integrate intensity of defect related peak areas for C@DZ/N were higher than the Co₉S₈@defective ZnS, confirming the vacancies increased in C@DZ/N. Meanwhile, the O1s peaks of Co₉S₈@defective ZnS and C@DZ/N revealed red shifts compared to the Co₉S₈@ZnS, which should be attributed to the hydroxyl groups and oxygen bounded to the surface defects after defect engineering of ZnS [43,44]. On the other hand, after donating the electrons to defective ZnS, a new peak of Co 2p was observed at 778.74 eV after the formation of defect (Fig. 2f), which indicated the valence state of Co element on its surface was oxidized to create a more electron-rich and conductive nanocubic surface [45].

3.2. Structural and photoelectric properties of cascade Z-scheme heterojunction in C@DZ/N

Upon the fabrication of ternary heterogeneous system, we hypothesize the charge transfer could be significantly improved by the cascade Z-scheme heterojunction, in which an efficient energy-transfer platform for direct charge transfer and separation was constructed and the formation will be discussed later (Fig. 3a). In general, defect engineering was used to introduce mid gap states in the bandgaps to alter the energy band structure and charge separation for matching the cascade heterostructures [33,46]. Therefore, to explore more details of specific defect engineering on heterojunction construction, Raman spectra of each combination with defective ZnS were characterized and analyzed. As shown in Fig. 3b, the same region of 210–240 cm⁻¹ verifies the second-order Raman peak of sphalerite ZnS in the Co₉S₈@defective ZnS, defective ZnS/g-C₃N₄ and C@DZ/N. However, the C@DZ/N clearly shows strong first-order scattering peaks at 281.68 cm⁻¹ and 348.36 cm⁻¹, which corresponded to the transverse optical (TO) mode and longitudinal optical (LO) phonons in defective ZnS, respectively. Moreover, two intermediate peaks related to lattice defects appeared at 302.23 and 340.82 cm⁻¹, where the former manifests disorderly induced phonon mode at X-W-L, and the latter represents surface optical phonons (SO) caused by the destruction of surface symmetry [47]. Defect related Raman scatterings for Co₉S₈@defective ZnS and defective ZnS/g-C₃N₄ were observed with a large Raman shift (Fig. S5), implied lattice defects in C@DZ/N were more significant to match the bandgap and energy of heterojunction. Furthermore, the small peaks of C@DZ/N in PL were ascribed to the significant defective ZnS (Fig. 3c). Generally, defective ZnS can be divided into two groups, one for equivalent localized donor states including sulfur vacancies (Vs) and interstitial zinc atoms (Iz), the other for acceptor states including zinc vacancies (Vz) and interstitial sulfur (Is) sites (Fig. 3d) [48]. Here, the broad peak at 517 nm with an equivalent energy gap of 2.26 eV was

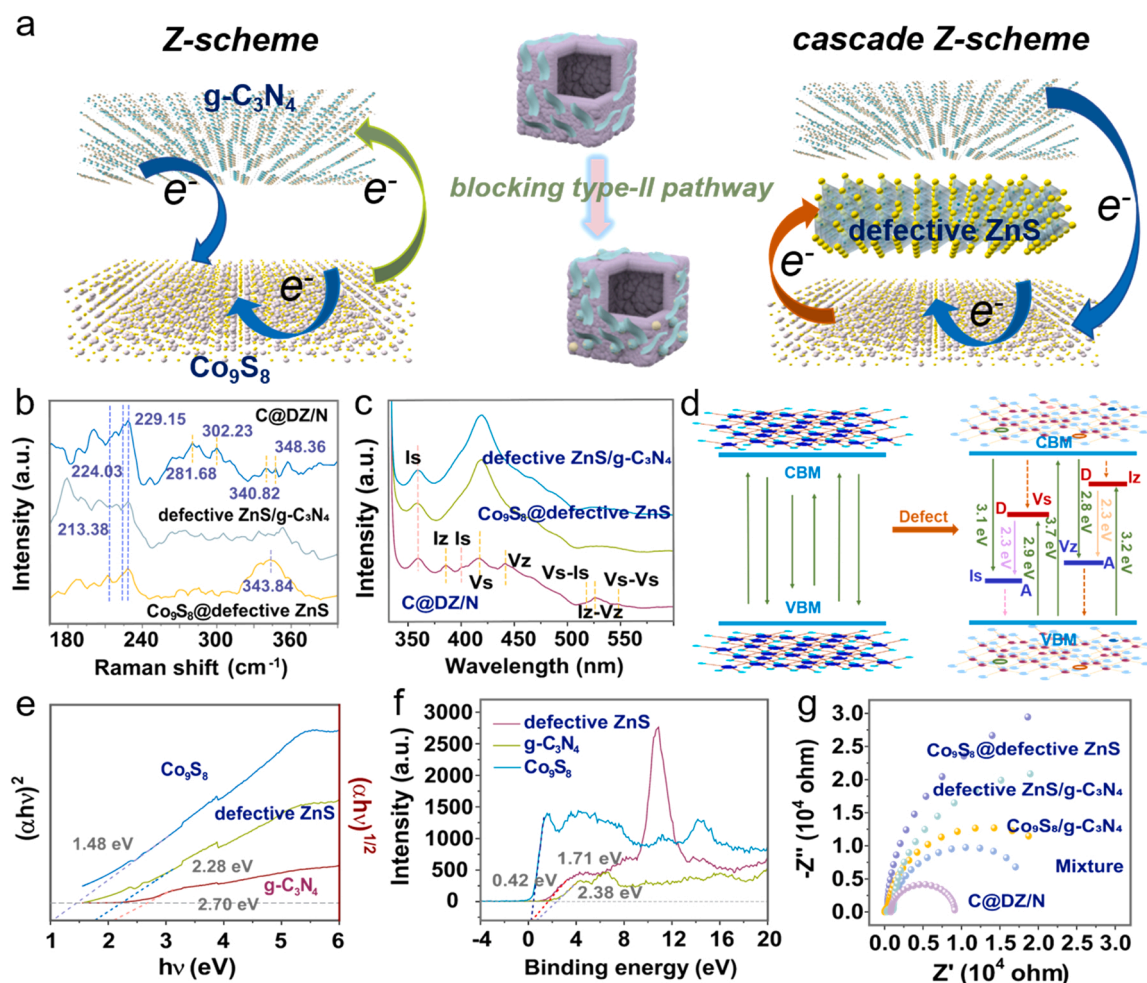


Fig. 3. Defect engineering design and photoelectric properties of cascade Z-scheme heterojunction. (a) Schematic of the charge transfer pathways for Co₉S₈/g-C₃N₄ and C@DZ/N; (b) Raman spectra of Co₉S₈ @defective ZnS, defective ZnS/g-C₃N₄ and C@DZ/N; (c) PL spectra of the defective ZnS, Co₉S₈ @defective ZnS, and C@DZ/N; (d) the relative energy levels of defective ZnS; (e) the corresponding Tauc plots and (f) VB XPS of the Co₉S₈, defective ZnS and g-C₃N₄; (g) EIS spectra of the Co₉S₈ @defective ZnS, defective ZnS/g-C₃N₄, Co₉S₈/g-C₃N₄, the mixture (Co₉S₈/g-C₃N₄ and Co₉S₈ @defective ZnS), and C@DZ/N.

ascribed to the de-trap recombination process from Vs level to Is level, and the peak at 530 nm was attributed to the interband recombination between Iz and Vz energy levels, which was consistent with the reports of relative energy levels of defective ZnS [48,49]. Those phenomena implied the successful construction of cascade Z-scheme heterojunction structures of C@DZ/N.

Compared to the Z-scheme heterojunction, the charge migration pathways of cascade Z-scheme heterojunction could inhibit the competitive type II heterojunctions effectively, which the introduced additional energy platforms by defect engineering of ZnS could promote photogenerated electrons timely transferred as well as accelerate photocarrier separation and transfer. Therefore, to validate these properties, a series of experiments were conducted in-depth. As shown in Fig. S6, the Co₉S₈/g-C₃N₄ exhibited higher absorption edge in comparison with g-C₃N₄, suggested the absorption scope could be improved by the Z-scheme heterojunction. Compared to the Co₉S₈/g-C₃N₄, the absorption edge of C@DZ/N (593 nm) displayed a red shift to the visible region, which presented an increased light absorption capacity. Furthermore, the band gap structure of Co₉S₈ nanocube and g-C₃N₄ are estimated to be 1.48 eV and 2.70 eV by Tauc graph, respectively (Fig. 3e). The Eg of the defective ZnS is 2.28 eV, which is narrower than that of ZnS (3.7 eV) [38]. Besides, the VB (valence band) of the Co₉S₈, defective ZnS and g-C₃N₄ are + 0.42 eV, + 1.71 eV and + 2.38 eV by the VB XPS energy spectra, respectively (Fig. 3f). Meanwhile, the Eg in the sample of C@DZ/N (1.15 eV) was narrower than that of the Co₉S₈ (1.48 eV) and

Co₉S₈/g-C₃N₄ (1.43 eV), indicating the cascade Z-scheme heterojunction of C@DZ/N was much easier to produce photo-excited carriers under the same visible light-induced energy (Figs. S6b and S7). Based on the obtained results, the strong evidences were provided by matching the energy bands of the cascaded heterojunctions structure, where the defective ZnS acted as interfacial “bridges” connect with Co₉S₈ through chemical bonds, and the Z-scheme charge transfer pathway could be significantly improve [34]. Specially, defective ZnS could also prolong the lifetimes of spatially separated electrons and holes by pumped out the electrons in the CB of Co₉S₈ [33].

For the photocarrier separation and transfer, here, the C@DZ/N showed best efficiency of photocarrier separation due to the lowest PL intensity, which could be attributed to the cascade Z-scheme heterojunction facilitate the photocarriers separation (Fig. 3c). Furthermore, the electrochemical impedance in Fig. 3g, displayed the C@DZ/N with lower charge transfer resistance than other components, where the diameter of the semicircle were corresponded to this property, manifesting the cascade Z-scheme heterojunction decreased the interfacial charge transfer resistance, in turn promoted the photogenerated carriers transfer and separation [34]. In addition, Fig. S8 shows the data of visible light-driven photocurrent response, where the photocurrent of C@DZ/N increased to the value of 10.65 μ A, indicated the better accelerated photocarriers separation and migration efficiency than Co₉S₈/g-C₃N₄. All of these demonstrated the cascade Z-scheme heterostructure of C@DZ/N can promote the charge separation and transfer

through strengthening the typical Z-Scheme charge pathway [50,51].

3.3. Photocatalytic performance and mechanism study of C@DZ/N toward Cr(VI) and CIP

The cascaded Z-scheme structure of charge transfer and separation was proposed in Fig. 4a, where an effective strategy for improving ROS generation was depicted through steering electron migration pathways. For common Z-scheme pathway, the photoinduced electrons at the CB of g-C₃N₄ will recombine with holes present in the VB of Co₉S₈. The strong holes left in the VB of g-C₃N₄ induce water oxidation to generate ROS, and the photogenerated electrons of Co₉S₈ CB initiate a reduction reaction (Fig. S9). However, the charge transfer pathway of C@DZ/N occurred from the CB of Co₉S₈ to the additional energy platform of introduced defective ZnS, which suppressed the recombination between electrons and Co₉S₈, and prolonged the lifetime of photogenerated electrons simultaneously [30]. Therefore, this transfer pathway of photogenerated electrons can promote the ROS generation of reduction reaction on the cascaded Z-scheme heterojunction [E_0 ($O_2/\cdot O_2^-$) = -0.33 V vs NHE] [52]. Furthermore, the interfacial interactions of cascaded Z-Scheme heterojunction maintained the redox potential as strong as possible and prolonged the carriers lifetime by blocking the type-II heterojunction, leading to more ROS generation through water oxidation subsequently [33]. Therefore, the generation of 1O_2 [E_0 ($O_2/{}^1O_2$) = +1.88 eV vs NHE] and $\cdot OH$ [E_0 ($\cdot OH/H_2O$) = +2.34 eV vs NHE] could be enhanced significantly by the efficient photogenerated holes transfer pathway [10].

CIP and Cr(VI) as hard-to-degrade pollutants in environment were selected as removal models to evaluate the photocatalytic activity of C@DZ/N. The photocatalytic removal performance of different

components for each pollutant were compared in detail. For CIP, as shown in Fig. 4b, degradation efficiency of C@DZ/N was higher than that of Co₉S₈, Co₉S₈ @defective ZnS, Co₉S₈/g-C₃N₄ and the mixture, where the removal efficiency of C@DZ/N could be achieved 97.01 % at 120 min. Moreover, the kinetic degradation rate of C@DZ/N for CIP was calculated to be 0.0149 min⁻¹, which was increased by \approx 11-fold and \approx 5-fold compared with those of Co₉S₈ @defective ZnS and Co₉S₈/g-C₃N₄, respectively (Fig. S10). For Cr(VI), C@DZ/N showed the highest photocatalytic activity (96.13 % reduction in 100 min), and the quasi-first order rate constant (k) was calculated to be 0.0149 min⁻¹, which was more than 3-fold of Co₉S₈/g-C₃N₄ (0.00441 min⁻¹). Specifically, the photocatalytic reduction in C@DZ/N was significantly improved approximately 25 % compared with the mixture of Co₉S₈/g-C₃N₄ and Co₉S₈ @defective ZnS, indicating the formation of cascade heterojunction accelerates the charge transfer and separation efficiency of photo-generated holes. For the reusability study, Fig. 4f shows that the C@DZ/N could maintain excellent photocatalytic activity after five cycles in CIP and Cr(VI) solution. Furthermore, the XRD and XPS characterization were carried out after five cycles. No noticeable change in the XRD spectrum manifested the high stability of C@DZ/N (Fig. S12). Moreover, the good stability could also be validated by XPS results where the lattice and defect peaks of Zn 2p and S 2p were still maintained (Fig. S13). The peaks of Zn adjacent to the vacancy (1022.47 and 1045.17 eV) and S vacancy (162.66 eV) were slightly shifted to higher level, demonstrated the decreased surface electron cloud densities of Zn and S atoms in C@DZ/N, which was ascribed to the participation of vacancy in the photocatalytic reaction [40,53].

To interpret the underlying degradation mechanism, corresponding experiments and characterization were conducted. As shown in Fig. 4d, the presence of O₂ had a greater impact on the C@DZ/N, and the

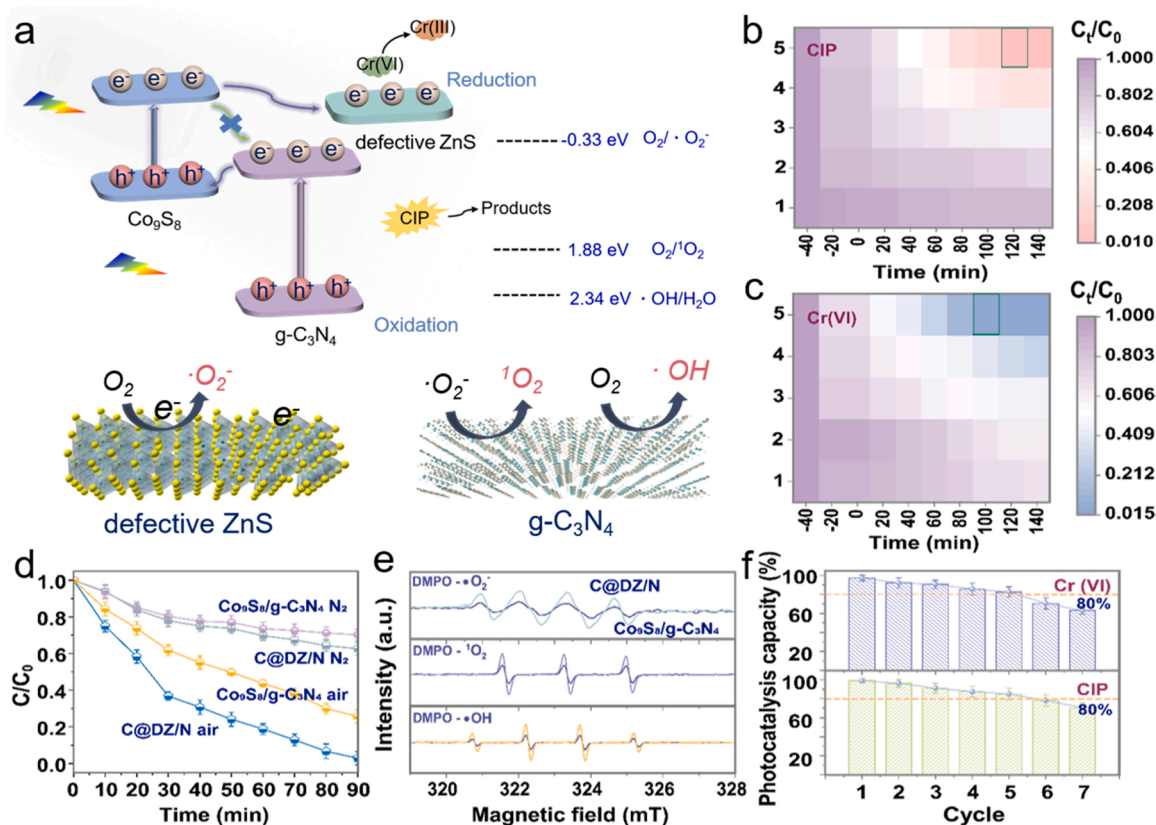


Fig. 4. Photocatalytic performance and mechanism of C@DZ/N toward Cr(VI) and CIP. (a) Schematic diagram for the photocatalytic mechanism and electron transfer mechanisms of cascade Z-scheme heterojunction; Comparison of degradation of CIP (b) and Cr (c) by 1) Co₉S₈, 2) Co₉S₈ @defective ZnS, 3) Co₉S₈/g-C₃N₄, 4) the mixture and 5) C@DZ/N; (d) CIP degradation of C@DZ/N and Co₉S₈/g-C₃N₄ under aerobic and anaerobic conditions; (e) the ESR spectra of DMPO- $\cdot O_2$, DMPO- $\cdot {}^1O_2$ and DMPO- $\cdot OH$ towards Co₉S₈/g-C₃N₄ and C@DZ/N; (f) Cycles of photocatalytic removal of C@DZ/N towards Cr(VI) and CIP.

degradation efficiency of the $\text{Co}_9\text{S}_8/\text{g-C}_3\text{N}_4$ and C@DZ/N were inhibited in N_2 atmosphere. This could be attributed to the C@DZ/N had generated more ROS in air atmosphere during photocatalytic degradation. Furthermore, ESR was applied to verify this phenomenon. In Fig. 4e, all the three free radicals including $\cdot\text{O}_2$, $^1\text{O}_2$ and $\cdot\text{OH}$ in C@DZ/N increased about 2 times compared with $\text{Co}_9\text{S}_8/\text{g-C}_3\text{N}_4$, which implied the cascade Z-Scheme charge transfer between $\text{Co}_9\text{S}_8/\text{g-C}_3\text{N}_4$ and defective ZnS achieve more photoelectrons for reduction of O_2 , rather than the common Z-scheme charge transfer. In addition, according to the ESR data, the electron transfer from ZnS to $\text{g-C}_3\text{N}_4$ has been excluded due to the CB of $\text{g-C}_3\text{N}_4$ was situated under the potential of $\text{O}_2/\cdot\text{O}_2$.

3.4. Multi-pollutants removal and mechanism study

To study the removal performance of C@DZ/N in multi-pollutants environment, a series of experiments under the co-exist of CIP and Cr(VI) were carried out. As shown in Fig. 5a, with the coexistence of CIP and Cr(VI), the degradation abilities of C@DZ/N were enhanced to 98.93 % compared to the other compositions (41.92 % for $\text{Co}_9\text{S}_8/\text{g-C}_3\text{N}_4$, 26.28 % for Co_9S_8 @defective ZnS, and 68.61 % for the mixture), especially exhibited 2-fold improvement compared to the Z-scheme heterojunction $\text{Co}_9\text{S}_8/\text{g-C}_3\text{N}_4$. Moreover, the CIP and Cr(VI) could be completely degraded after 90 min with the existence of C@DZ/N under visible light (Fig. 5b and c). The removal efficiency of Cr(VI) was not

particularly enhanced in multi-pollutants compared with single-pollutant environment. However, the degradation efficiency of CIP significantly improved in multi-pollutants environment. Moreover, unlike the common Z-scheme in $\text{TiO}_2/\text{g-C}_3\text{N}_4$ and ternary heterojunction in CBM, the C@DZ/N exhibited better photodegradation rate for CIP, which ascribed to the optimized charge transfer pathway of cascade Z-scheme heterojunction that facilitated CIP degradation by directional conversion of ROS (Table S3).

For in-depth analyze these phenomena, the quenching experiment was carried out to reveal the critical effect of ROS. As shown in Fig. 5d, the Cr(VI) reduction efficiency decreased with the addition of LAA, which indicated the e^- is the only free radical in the reduction of Cr(VI). With the addition of TBA and TEMP, the removal efficiency of CIP was significantly reduced, indicating that $\cdot\text{OH}$ and $^1\text{O}_2$ are the active substances for CIP removal. However, the removal efficiency of CIP after the addition of BQ was slightly raised, which demonstrated that the sacrifice of $\cdot\text{O}_2$ may have a promoting effect on producing other ROS [45], that in turn facilitate CIP degradation in multi-pollutants environment.

Based on the above experimental results, the enhanced photocatalytic removal efficiency mechanism in multi-pollutants environment was illustrated. From the Co 2p spectra after removal in Fig. 5f, after the generation of ROS, the atom percentages of Co^{3+} (the peak at 778.74 eV) increased from 3.76 % to 32.52 % indicated the photoreduction reaction created a more electron-rich and conductive surface on

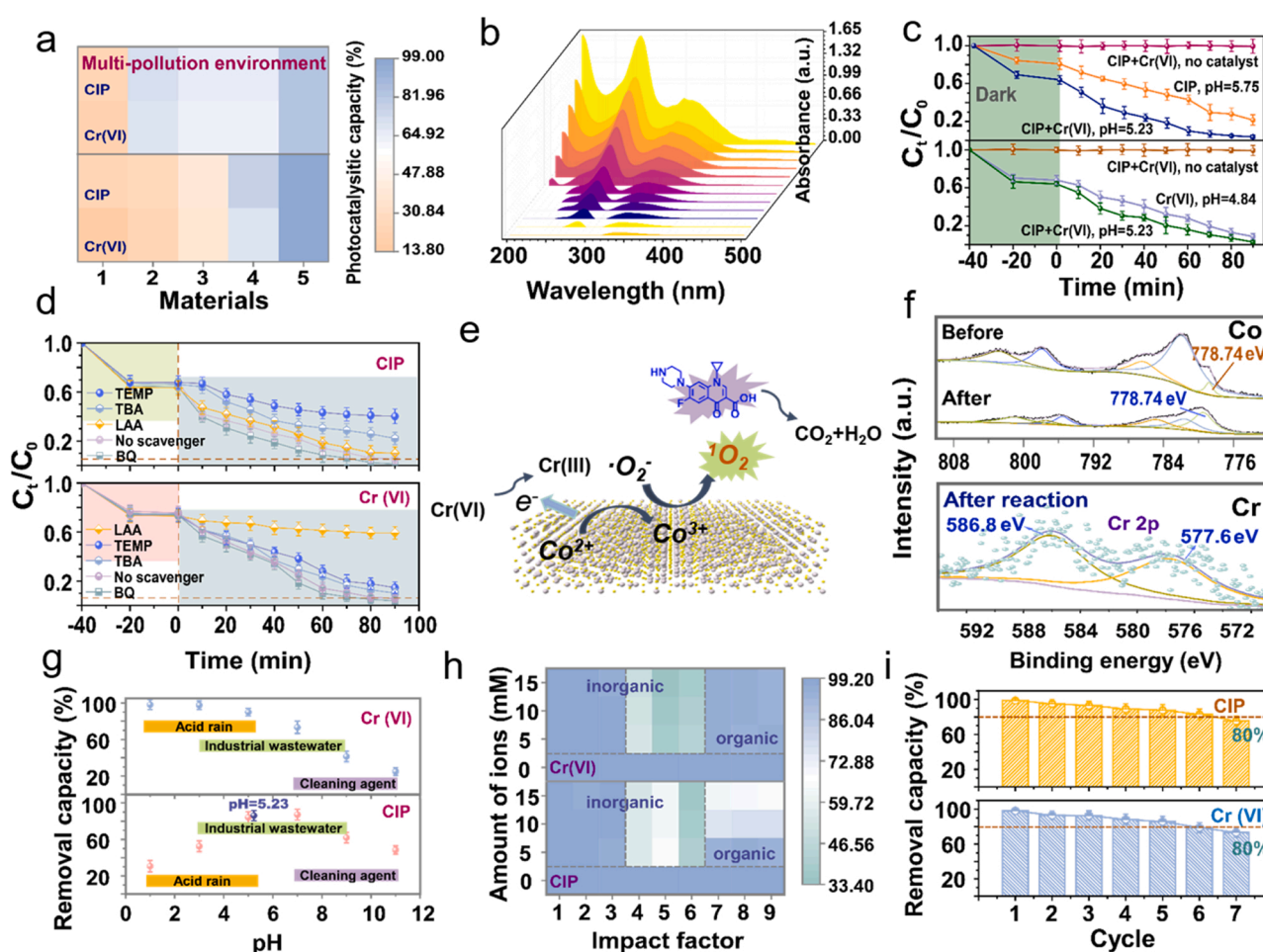


Fig. 5. Multi-pollutants removal and mechanism study of C@DZ/N . (a) Photocatalytic performance of 1) Co_9S_8 , 2) Co_9S_8 @defective ZnS, 3) $\text{Co}_9\text{S}_8/\text{g-C}_3\text{N}_4$, 4) the mixture, 5) C@DZ/N ; (b) time-dependent removal spectral pattern of CIP and Cr(VI) solutions over C@DZ/N ; (c) removal performance of C@DZ/N towards CIP (up) and Cr(VI) (down) in different pollutant system; (d) multi-pollutants removal performance of C@DZ/N with different ROS scavengers; (e) schematic diagram to show the multi-pollutants removal mechanism of C@DZ/N ; (f) high-resolution Co and Cr spectra of C@DZ/N before and after multi-pollutants removal; (g) influence of pH values on multi-pollutants removal capacities over C@DZ/N ; (h) interference of 1) NaCl, 2) MgSO_4 , 3) KNO_3 , 4) NH_4Cl , 5) Na_2CO_3 , 6) KH_2PO_4 , 7) TC-HCl, 8) LEV and 9) BPA on multi-pollutants removal over C@DZ/N ; (i) removal capacities of CIP and Cr(VI) over C@DZ/N in cyclic multi-pollutants removal.

C@DZ/N [34], which verifies valence fluctuation of Co promoted the ROS directional conversion [45,54]. The enhanced mechanism in multi-pollutants environment was illustrated as follow: O₂ could reduce to O₂^{•−} through a one-electron process serving as reactive sites [Eq. (1)] [55]; O₂ was then, quickly oxidized to the key active species ¹O₂ by the highly oxidizing Co³⁺ exposed on the surface of C@DZ/N [Eq. (2)], thus in turn facilitate CIP degradation in multi-pollutants environment [45, 56].



Through the charge migration from the photoreduction of Cr(VI), the surface of Co₉S₈ with enhanced electrophilicity increased the adsorption capacity of ROS, and promoted the directional conversion of ROS by continuous charge transfer (Fig. 5e). The detailed ROS generation processes on Co₉S₈ surface displayed that O₂ was then quickly oxidized to ¹O₂ by the highly oxidizing Co³⁺, which exposed on the surface of C@DZ/N. Based on the above analysis, the valence fluctuation of C@DZ/N surface promoted the directional conversion of main ROS to achieve the significantly enhanced photodegradation efficiency in multi-pollutants system.

The photocatalytic efficiencies of CIP degradation were found to be pH-dependent and to exhibit a maximum value at around pH 5–7 due to the different dominant dissociation forms of CIP [57]. And the existence of Cr(VI) could lead to the variation of the pH environment in CIP. Therefore, to further verified the synergy effect of C@DZ/N in multi-pollutants environments, we compared the CIP degradation efficiency in the solution of CIP+H⁺ and multi-pollutants. As shown in Fig. 5c and g, the degradation efficiency of CIP in multi-pollutants was significantly increased than CIP+H⁺, which excluded the pH effect to the degradation process of CIP, thus imply the enhanced degradation efficiency of CIP could result from the participation of ROS in multi-pollutants system. To investigate the influence of different substances on photocatalytic process, experimental studies were conducted on interferences such as inorganic ions and organic matter. As shown in Fig. 5 h and Fig. S15, the effects of NaCl, MgSO₄ and KNO₃ on the photocatalytic activity of C@DZ/N are basically negligible. However, the photocatalytic redox efficiency of C@DZ/N on both of CIP and Cr(VI) decreases with the increase of the concentration of NH₄Cl, Na₂CO₃ and KH₂PO₄, indicating that the reduced photocatalytic activity may be due to the competition between pollutants and ions for active sites (NH₄⁺ and CO₃^{2−} leading to pH changed, and competition existed between reactions with H₂PO₄[−] or CO₃^{2−}). As shown in Fig. 5 h and S13, C@DZ/N was provided with good photodegradation property for LEV (levofloxacin), BPA (bisphenol A) and TC-HCl (tetracycline hydrochloride), and the efficiencies of LEV, BPA and TC-HCl were 84.86 %, 82.19 % and 86.41 %, respectively. The kinetics of LEV, BPA and TC-HCl photocatalytic degradation over all catalysts were fitted, and all samples conformed to the first-order kinetics model. The photocatalytic CIP degradation rate of C@DZ/N was calculated to be 0.0149 min^{−1}, which was 1.72, 1.76 and 1.64 times higher than that of LEV, BPA, TC-HCl, respectively (Fig. S16). In addition, to verify the stability of C@DZ/N in multi-pollutants system, the removal capacities of CIP and Cr(VI) during five consecutive cycles were still above 80 % shown in Fig. 5i.

3.5. Evaluation of photocatalytic intermediates of CIP in multi-pollutants system

In order to clarify the removal of CIP and Cr(VI) reduction products in the C@DZ/N photocatalytic process, LC-MS and XPS were used to analysis. For Cr(VI), as shown in Fig. 5 f, Cr was found in the full-measured XPS spectrum of C@DZ/N after photocatalysis. The high-resolution XPS spectrum of Cr 2p was divided into two peaks at 577.3 eV and 587.0 eV, which were designated as Cr(III) and demonstrated the Cr(VI) was reduced during photocatalytic degradation [58,

59]. For CIP, based on the LC-MS spectrum, the intermediates of CIP in the photocatalytic process were depicted in Fig. 6 and Table S4, and the corresponding mass spectrometry (MS) and secondary mass spectrometry (MS²) were summarized In Table S5 [6,10,60–62]. As shown in Fig. 6, the photodegradation of CIP initiated in four main photo-reaction paths via oxidation of ·OH and ¹O₂. In the degradation pathway 1, ·OH reacts with CIP to form an ·OH-adduct, producing a series of hydroxylated products of C1, C2 and C3 on aromatic rings, with another hydroxyl radical addition to the parent molecule, while the F atom is also substituted with a hydroxyl radical by attack of OH to -F. After decarboxylation, C4 was oxidized, corresponding to the breakdown of its quinolone ring. In pathway 4, the pyrrole ketone ring opening process by ·OH attacked C14. Of course, all the early intermediates and the hydroxylation intermediates would result in the breakdown of their quinolone ring structures with the further progress of degradation [63,64]. On the other hand, the stepwise oxidation of the piperazine side chain of CIP through ¹O₂ results in the cleavage of C-C bonds and the addition of oxygen atom on the piperazine, with the generation of dialdehyde derivative C8 (pathway 3). Then, C8 is oxidized to C9 with mono-aldehyde moiety by the loss of formaldehyde group. Followed by the loss of the other formaldehyde group and secondary amine nitrogen of C9 lead to the formation of C10. And the pathway 2 is that the singlet oxygen attacked making the generation of C5 and C6 from different degrees of oxidation of piperazine rings. The generation of C7 may be attributed to the further loss of formaldehyde and the loss of amine nitrogen. From C7, the piperazine ring is completely opened. C11 is also a minimum molecular weight in all products, indicating that the piperazine ring cracking caused by the ¹O₂ generation is the main pathway in the degradation process [65–69]. Finally, the above intermediates could be degraded into CO₂, H₂O, F[−], NH₄⁺ and other molecules.

4. Conclusion

In summary, a cascade Z-scheme heterojunction photocatalyst in hollow cubic structure with the defects interface was constructed, which showed excellent photocatalytic activity in multi-pollutants environments. The performance of C@DZ/N for CIP degradation under visible light exhibits almost 5-fold better than pure Co₉S₈ nanocube, even superior nearly 2-fold to the mixture of individual components. All of these demonstrated the defective ZnS could act as an electron transfer platform to facilitate directional charge transfer between hollow Co₉S₈ and g-C₃N₄, which is critical for directing Z-Scheme charge transfer and separation for efficient ROS reaction. Importantly, this strategy is also suitable for promoting charge transfer in multi-pollutants system and provides a cubic surface oxidation for the enhanced ROS (¹O₂) production efficiency. This study demonstrates a facile strategy to design unique cascade Z-scheme defect-based heterojunction for efficient multi-pollutants degradation.

CRedit authorship contribution statement

Chengyuan Yang: Conceptualization, Methodology, Formal analysis, Investigation, Data curation, Writing – original draft. **Jing Wang:** Conceptualization, Validation, Writing – review & editing. **Rong Wang:** Validation, Manuscript checking. **Wenxin Zhu:** Validation, Manuscript checking. **Liang Zhang:** Investigation, Data curation, Methodology. **Ting Du:** Investigation, Data curation, Methodology. **Jing Sun:** Formal analysis, Investigation. **Ming-Qiang Zhu:** Formal analysis, Investigation. **Yizhong Shen, Jianlong Wang:** Supervision, Funding acquisition, Manuscript editing, Manuscript final version approval.

Declaration of Competing Interest

The authors declare that they have no known competing financial interests or personal relationships that could have appeared to influence the work reported in this paper.

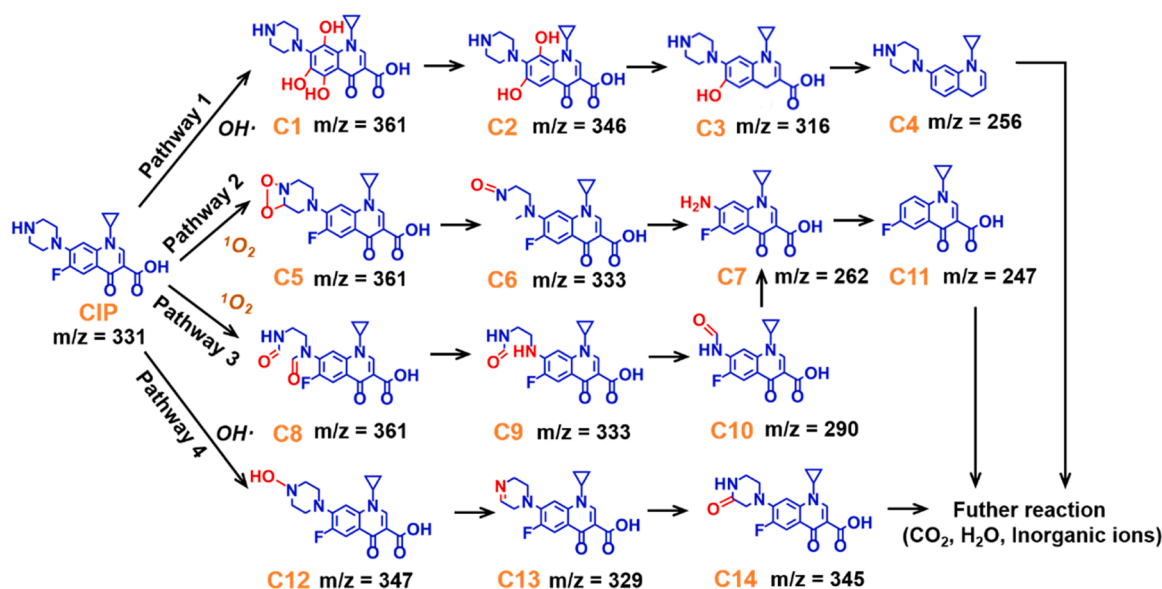


Fig. 6. Degradation pathways of CIP in multi-pollutants system over C@DZ/N.

Data availability

No data was used for the research described in the article.

Acknowledgements

The authors thank the National Key Research and Development Program of China (2018YFE0127000), National Natural Science Foundation of China (21675127), Shaanxi Provincial Science Fund for Distinguished Young Scholars (2018JC-011), Qinghai Special Project of Innovation Platform for Basic Conditions of Scientific Research of China (2022-ZJ-Y18). We thank Jingyan Li (College of Food Science and Engineering, Northwest A&F University, China) for her help in the detection of intermediates with LC-MS test. We also thank Guoyun Zhang (State Key Laboratory of Crop Stress Biology for Arid Areas, Northwest A&F University, China) for his experimental assistance with SEM test and analysis.

Appendix A. Supporting information

Supplementary data associated with this article can be found in the online version at [doi:10.1016/j.apcatb.2022.122084](https://doi.org/10.1016/j.apcatb.2022.122084).

References

- [1] M. Mon, R. Bruno, E. Tiburcio, M. Viciano-Chumillas, L.H.G. Kalinke, J. Ferrando-Soria, D. Armentano, E. Pardo, Multivariate metal-organic frameworks for the simultaneous capture of organic and inorganic contaminants from water, *J. Am. Chem. Soc.* 141 (2019) 13601–13609.
- [2] S. Yu, X. Wang, H. Pang, R. Zhang, W. Song, D. Fu, T. Hayat, X. Wang, Boron nitride-based materials for the removal of pollutants from aqueous solutions: a review, *Chem. Eng. J.* 333 (2018) 343–360.
- [3] J. Li, X. Wang, G. Zhao, C. Chen, Z. Chai, A. Alsaedi, T. Hayat, X. Wang, Metal-organic framework-based materials: superior adsorbents for the capture of toxic and radioactive metal ions, *Chem. Soc. Rev.* 47 (2018) 2322–2356.
- [4] Y. Liu, H. Mou, L. Chen, Z.A. Mirza, L. Liu, Cr (VI)-contaminated groundwater remediation with simulated permeable reactive barrier (PRB) filled with natural pyrite as reactive material: environmental factors and effectiveness, *J. Hazard. Mater.* 298 (2015) 83–90.
- [5] Q. Zhang, M. Wang, M. Ao, Y. Luo, A. Zhang, L. Zhao, L. Yan, F. Deng, X. Luo, Solvothermal synthesis of Z-scheme AgInS₂/Bi₂WO₆ nano-heterojunction with excellent performance for photocatalytic degradation and Cr (VI) reduction, *J. Alloy. Compd.* 805 (2019) 41–49.
- [6] Y. Wang, L. Rao, P. Wang, Z. Shi, L. Zhang, Photocatalytic activity of N-TiO₂/O-doped N vacancy g-C₃N₄ and the intermediates toxicity evaluation under tetracycline hydrochloride and Cr(VI) coexistence environment, *Appl. Catal. B Environ.* 262 (2020).
- [7] F. Chen, Q. Yang, Y. Wang, F. Yao, Y. Ma, X. Huang, X. Li, D. Wang, G. Zeng, H. Yu, Efficient construction of bismuth vanadate-based Z-scheme photocatalyst for simultaneous Cr(VI) reduction and ciprofloxacin oxidation under visible light: kinetics, degradation pathways and mechanism, *Chem. Eng. J.* 348 (2018) 157–170.
- [8] Y. Zhou, T. Cai, S. Liu, Y. Liu, H. Chen, Z. Li, J. Du, Z. Lei, H. Peng, N-doped magnetic three-dimensional carbon microspheres@TiO₂ with a porous architecture for enhanced degradation of tetracycline and methyl orange via adsorption/photocatalysis synergy, *Chem. Eng. J.* 411 (2021).
- [9] M. Guo, Z. Xing, T. Zhao, Z. Li, S. Yang, W. Zhou, WS₂ quantum dots/MoS₂@WO_{3-x} core-shell hierarchical dual Z-scheme tandem heterojunctions with wide-spectrum response and enhanced photocatalytic performance, *Appl. Catal. B Environ.* 257 (2019).
- [10] Y. Zhou, M. Yu, H. Liang, J. Chen, L. Xu, J. Niu, Novel dual-effective Z-scheme heterojunction with g-C₃N₄, Ti₃C₂ MXene and black phosphorus for improving visible light-induced degradation of ciprofloxacin, *Appl. Catal. B Environ.* 291 (2021).
- [11] Z. Cheng, L. Ling, Z. Wu, J. Fang, P. Westerhoff, C. Shang, Novel visible light-driven photocatalytic chlorine activation process for carbamazepine degradation in drinking water, *Environ. Sci. Technol.* 54 (2020) 11584–11593.
- [12] Y.-H. Chiu, T.-F.M. Chang, C.-Y. Chen, M. Sone, Y.-J. Hsu, Mechanistic insights into photodegradation of organic dyes using heterostructure photocatalysts, *Catalysts* 9 (2019) 430.
- [13] M.-J. Fang, C.-W. Tsao, Y.-J. Hsu, Semiconductor nanoheterostructures for photoconversion applications, *J. Phys. D Appl. Phys.* 53 (2020), 143001.
- [14] C.-W. Tsao, M.-J. Fang, Y.-J. Hsu, Modulation of interfacial charge dynamics of semiconductor heterostructures for advanced photocatalytic applications, *Coord. Chem. Rev.* 438 (2021), 213876.
- [15] K. Wang, Z. Xing, M. Du, S. Zhang, Z. Li, K. Pan, W. Zhou, Hollow MoSe₂/Bi₂S₃/CdS core-shell nanostructure as dual Z-scheme heterojunctions with enhanced full spectrum photocatalytic-photothermal performance, *Appl. Catal. B Environ.* 281 (2021).
- [16] D. Zu, H. Song, Y. Wang, Z. Chao, Z. Li, G. Wang, Y. Shen, C. Li, J. Ma, One-pot in-situ hydrothermal synthesis of CdS/Nb₂O₅/Nb₂C heterojunction for enhanced visible-light-driven photodegradation, *Appl. Catal. B Environ.* 277 (2020).
- [17] L. Zhang, J. Wang, H. Wang, W. Zhang, W. Zhu, T. Du, Y. Ni, X. Xie, J. Sun, J. Wang, Rational design of smart adsorbent equipped with a sensitive indicator via ligand exchange: a hierarchical porous mixed-ligand MOF for simultaneous removal and detection of Hg²⁺, *Nano Res.* 14 (2021) 1523–1532.
- [18] T. Liu, D. Zhang, K. Yin, C. Yang, S. Luo, J.C. Crittenden, Degradation of thiachlorid via unactivated peroxymonosulfate: the overlooked singlet oxygen oxidation, *Chem. Eng. J.* 388 (2020), 124264.
- [19] S. Zhu, X. Li, J. Kang, X. Duan, S. Wang, Persulfate activation on crystallographic manganese oxides: mechanism of singlet oxygen evolution for nonradical selective degradation of aqueous contaminants, *Environ. Sci. Technol.* 53 (2018) 307–315.
- [20] P. Zhang, X.W. Lou, Design of heterostructured hollow photocatalysts for solar-to-chemical energy conversion, *Adv. Mater.* 31 (2019).
- [21] B. Qiu, Q. Zhu, M. Du, L. Fan, M. Xing, J. Zhang, Efficient solar light harvesting CdS/Co₉S₈ hollow cubes for Z-scheme photocatalytic water splitting, *Angew. Chem. Int. Ed.* 56 (2017) 2684–2688.
- [22] G. Zhang, D. Chen, N. Li, Q. Xu, H. Li, J. He, J. Lu, Construction of hierarchical hollow Co₉S₈/ZnIn₂S₄ tubular heterostructures for highly efficient solar energy conversion and environmental remediation, *Angew. Chem. Int. Ed.* 59 (2020) 8255–8261.

- [23] S. Wang, B.Y. Guan, X. Wang, X.W.D. Lou, Formation of hierarchical $\text{Co}_3\text{S}_8@ \text{ZnIn}_2\text{S}_4$ heterostructured cages as an efficient photocatalyst for hydrogen evolution, *J. Am. Chem. Soc.* 140 (2018) 15145–15148.
- [24] Y.-A. Chen, Y.-T. Wang, H.S. Moon, K. Yong, Y.-J. Hsu, Yolk-shell nanostructures: synthesis, photocatalysis and interfacial charge dynamics, *RSC Adv.* 11 (2021) 12288–12305.
- [25] Y. Wei, N. Yang, K. Huang, J. Wan, F. You, R. Yu, S. Feng, D. Wang, Steering hollow multishelled structures in photocatalysis: optimizing surface and mass transport, *Adv. Mater.* 32 (2020).
- [26] Y.Z. Wang, M. Yang, Y.M. Ding, N.W. Li, L. Yu, Recent advances in complex hollow electrocatalysts for water splitting, *Adv. Funct. Mater.* 32 (2022), 2108681.
- [27] M. Guo, Z. Xing, T. Zhao, Y. Qiu, B. Tao, Z. Li, W. Zhou, Hollow flower-like polyhedral $\alpha\text{-Fe}_2\text{O}_3/\text{Defective MoS}_2/\text{Ag}$ Z-scheme heterojunctions with enhanced photocatalytic-Fenton performance via surface plasmon resonance and photothermal effects, *Appl. Catal. B Environ.* 272 (2020).
- [28] A. Kumar, G. Sharma, A. Kumari, C. Guo, M. Naushad, D.-V.N. Vo, J. Iqbal, F. J. Stadler, Construction of dual Z-scheme $\text{g-C}_3\text{N}_4/\text{Bi}_4\text{Ti}_3\text{O}_{12}/\text{Bi}_4\text{O}_5\text{I}_2$ heterojunction for visible and solar powered coupled photocatalytic antibiotic degradation and hydrogen production: Boosting via I^-/I_3^- and $\text{Bi}^{3+}/\text{Bi}^{5+}$ redox mediators, *Appl. Catal. B Environ.* 284 (2021).
- [29] W. Li, X. Wang, Q. Ma, F. Wang, X.-s. Chu, X.-c. Wang, C.-y. Wang, CdS@h-BN heterointerface construction on reduced graphene oxide nanosheets for hydrogen production, *Appl. Catal. B Environ.* 284 (2021).
- [30] J. Bian, Z. Zhang, J. Feng, M. Thangamuthu, F. Yang, L. Sun, Z. Li, Y. Qu, D. Tang, Z. Lin, F. Bai, J. Tang, L. Jing, Energy platform for directed charge transfer in the cascade Z-scheme heterojunction: CO_2 photoreduction without a cocatalyst, *Angew. Chem. Int. Ed.* 60 (2021) 20906–20914.
- [31] J. Low, B. Dai, T. Tong, C. Jiang, J. Yu, In situ irradiated X-ray photoelectron spectroscopy investigation on a direct Z-scheme TiO_2/CdS composite film photocatalyst, *Adv. Mater.* 31 (2019), 1802981.
- [32] P. Wang, Y. Mao, L. Li, Z. Shen, X. Luo, K. Wu, P. An, H. Wang, L. Su, Y. Li, Unraveling the interfacial charge migration pathway at the atomic level in a highly efficient Z-scheme photocatalyst, *Angew. Chem. Int. Ed.* 58 (2019) 11329–11334.
- [33] X. Wang, X. Wang, J. Huang, S. Li, A. Meng, Z. Li, Interfacial chemical bond and internal electric field modulated Z-scheme $\text{Sv-ZnIn}_2\text{S}_4/\text{MoSe}_2$ photocatalyst for efficient hydrogen evolution, *Nat. Commun.* 12 (2021).
- [34] N.K. Oh, J. Seo, S. Lee, H.-J. Kim, U. Kim, J. Lee, Y.-K. Han, H. Park, Highly efficient and robust noble-metal free bifunctional water electrolysis catalyst achieved via complementary charge transfer, *Nat. Commun.* 12 (2021).
- [35] X. Xu, J. Wang, T. Chen, N. Yang, S. Wang, X. Ding, H. Chen, Deep insight into ROS mediated direct and hydroxylated dichlorination process for efficient photocatalytic sodium pentachlorophenate mineralization, *Appl. Catal. B Environ.* 296 (2021).
- [36] N.S. Shah, J.A. Khan, M. Sayed, Z.U.H. Khan, H.S. Ali, B. Murtaza, H.M. Khan, M. Imran, N. Muhammad, Hydroxyl and sulfate radical mediated degradation of ciprofloxacin using nano zerovalent manganese catalyzed $\text{S}_2\text{O}_8^{2-}$, *Chem. Eng. J.* 356 (2019) 199–209.
- [37] R. Wu, D.P. Wang, X. Rui, B. Liu, K. Zhou, A.W.K. Law, Q. Yan, J. Wei, Z. Chen, In-situ formation of hollow hybrids composed of cobalt sulfides embedded within porous carbon polyhedra/carbon nanotubes for high-performance lithium-ion batteries, *Adv. Mater.* 27 (2015) 3038–3044.
- [38] J. Zhou, J. Zhao, R. Liu, Defect engineering of zeolite imidazole framework derived ZnS nanosheets towards enhanced visible light driven photocatalytic hydrogen production, *Appl. Catal. B Environ.* 278 (2020).
- [39] L. Shao, D. Jiang, P. Xiao, L. Zhu, S. Meng, M. Chen, Enhancement of $\text{g-C}_3\text{N}_4$ nanosheets photocatalysis by synergistic interaction of ZnS microsphere and RGO inducing multistep charge transfer, *Appl. Catal. B Environ.* 198 (2016) 200–210.
- [40] J. Zhao, X. Liu, X. Ren, X. Sun, D. Tian, Q. Wei, D. Wu, Defect-rich ZnS nanoparticles supported on reduced graphene oxide for high-efficiency ambient N_2 -to- NH_3 conversion, *Appl. Catal. B Environ.* 284 (2021).
- [41] X. Hao, Y. Wang, J. Zhou, Z. Cui, Y. Wang, Z. Zou, Zinc vacancy-promoted photocatalytic activity and photostability of ZnS for efficient visible-light-driven hydrogen evolution, *Appl. Catal. B Environ.* 221 (2018) 302–311.
- [42] T. Xu, P. Wang, D. Wang, K. Zhao, M. Wei, X. Liu, H. Liu, J. Cao, Y. Chen, H. Fan, Ultrasound-assisted synthesis of hyper-dispersed type-II tubular $\text{Fe}_3\text{O}_4@ \text{SiO}_2@ \text{ZnO}/\text{ZnS}$ core/shell heterostructure for improved visible-light photocatalysis, *J. Alloy. Compd.* 838 (2020), 155689.
- [43] M. Ayiania, M. Smith, A.J.R. Hensley, L. Scudiero, J.-S. McEwen, M. Garcia-Perez, Deconvoluting the XPS spectra for nitrogen-doped chars: an analysis from first principles, *Carbon* 162 (2020) 528–544.
- [44] Y.-P. Zhu, J. Li, T.-Y. Ma, Y.-P. Liu, G. Du, Z.-Y. Yuan, Sonochemistry-assisted synthesis and optical properties of mesoporous ZnS nanomaterials, *J. Mater. Chem. A* 2 (2014) 1093–1101.
- [45] J. Ji, Q. Yan, P. Yin, S. Mine, M. Matsuoka, M. Xing, Defects on CoS_2 -x: tuning redox reactions for sustainable degradation of organic pollutants, *Angew. Chem. Int. Ed.* 60 (2021) 2903–2908.
- [46] P. Nandi, D. Das, Photocatalytic degradation of Rhodamine-B dye by stable ZnO nanostructures with different calcination temperature induced defects, *Appl. Surf. Sci.* 465 (2019) 546–556.
- [47] Y.C. Cheng, C.Q. Jin, F. Gao, X.L. Wu, W. Zhong, S.H. Li, P.K. Chu, Raman scattering study of zinc blende and wurtzite ZnS, *J. Appl. Phys.* 106 (2009).
- [48] X. Wang, J. Shi, Z. Feng, M. Li, C. Li, Visible emission characteristics from different defects of ZnS nanocrystals, *Phys. Chem. Chem. Phys.* 13 (2011) 4715–4723.
- [49] A. Roychowdhury, S.P. Pati, S. Kumar, D. Das, Effects of magnetite nanoparticles on optical properties of zinc sulfide in fluorescent-magnetic $\text{Fe}_3\text{O}_4/\text{ZnS}$ nanocomposites, *Powder Technol.* 254 (2014) 583–590.
- [50] C. Liang, H.-P. Feng, H.-Y. Niu, C.-G. Niu, J.-S. Li, D.-W. Huang, L. Zhang, H. Guo, N. Tang, H.-Y. Liu, A dual transfer strategy for boosting reactive oxygen species generation in ultrathin Z-scheme heterojunction driven by electronic field, *Chem. Eng. J.* 384 (2020), 123236.
- [51] D. Xia, W. Wang, R. Yin, Z. Jiang, T. An, G. Li, H. Zhao, P.K. Wong, Enhanced photocatalytic inactivation of *Escherichia coli* by a novel Z-scheme $\text{g-C}_3\text{N}_4/\text{m-Bi}_2\text{O}_4$ hybrid photocatalyst under visible light: the role of reactive oxygen species, *Appl. Catal. B Environ.* 214 (2017) 23–33.
- [52] S. Swetha, B. Janani, S.S. Khan, A critical review on the development of metal-organic frameworks for boosting photocatalysis in the fields of energy and environment, *J. Clean. Prod.* (2021), 130164.
- [53] X. Hao, J. Zhou, Z. Cui, Y. Wang, Y. Wang, Z. Zou, Zn-vacancy mediated electron-hole separation in ZnS/g- C_3N_4 heterojunction for efficient visible-light photocatalytic hydrogen production, *Appl. Catal. B Environ.* 229 (2018) 41–51.
- [54] M. Kim, M.A.R. Anjum, M. Choi, H.Y. Jeong, S.H. Choi, N. Park, J.S. Lee, Covalent $^0\text{D}-^2\text{D}$ heterostructuring of $\text{Co}_3\text{S}_8\text{-MoS}_2$ for enhanced hydrogen evolution in all pH electrolytes, *Adv. Funct. Mater.* 30 (2020), 2002536.
- [55] W. Chen, Z. Sun, C. Jiang, W. Sun, B. Yu, W. Wang, L. Lu, An all-in-one organic semiconductor for targeted photoxidation catalysis in hypoxic tumor, *Angew. Chem. Int. Ed.* 133 (2021) 16777–16784.
- [56] J. Dong, L. Song, J.-J. Yin, W. He, Y. Wu, N. Gu, Y. Zhang, Co_3O_4 nanoparticles with multi-enzyme activities and their application in immunohistochemical assay, *ACS Appl. Mater. Interfaces* 6 (2014) 1959–1970.
- [57] X. Wei, J. Chen, Q. Xie, S. Zhang, L. Ge, X. Qiao, Distinct photolytic mechanisms and products for different dissociation species of ciprofloxacin, *Environ. Sci. Technol.* 47 (2013) 4284–4290.
- [58] Y. Wang, L. Rao, P. Wang, Z. Shi, L. Zhang, Photocatalytic activity of N-TiO₂/O-doped N vacancy g- C_3N_4 and the intermediates toxicity evaluation under tetracycline hydrochloride and Cr (VI) coexistence environment, *Appl. Catal. B Environ.* 262 (2020), 118308.
- [59] Y. Cui, M. Li, H. Wang, C. Yang, S. Meng, F. Chen, In-situ synthesis of sulfur doped carbon nitride microsphere for outstanding visible light photocatalytic Cr(VI) reduction, *Sep. Purif. Technol.* 199 (2018) 251–259.
- [60] X.-J. Wen, C.-G. Niu, L. Zhang, C. Liang, H. Guo, G.-M. Zeng, Photocatalytic degradation of ciprofloxacin by a novel Z-scheme $\text{CeO}_2\text{-Ag}/\text{AgBr}$ photocatalyst: influencing factors, possible degradation pathways, and mechanism insight, *J. Catal.* 358 (2018) 141–154.
- [61] P. Jiang, J. Qiu, Y. Gao, M.I. Stefan, X.-F. Li, Nontargeted identification and predicted toxicity of new byproducts generated from UV treatment of water containing micropollutant 2-mercaptobenzothiazole, *Water Res.* 188 (2021), 116542.
- [62] E.L. Schymanski, J. Jeon, R. Gulde, K. Fenner, M. Ruff, H.P. Singer, J. Hollender, Identifying small molecules via high resolution mass spectrometry: communicating confidence, *Environ. Sci. Technol.* (2014).
- [63] Y. Gao, X. Niu, Y. Qin, T. Guo, Y. Ji, G. Li, T. An, Unexpected culprit of increased estrogenic effects: oligomers in the photodegradation of preservative ethylparaben in water, *Water Res.* 176 (2020), 115745.
- [64] H. Fang, Y. Gao, G. Li, J. An, P.-K. Wong, H. Fu, S. Yao, X. Nie, T. An, Advanced oxidation kinetics and mechanism of preservative propylparaben degradation in aqueous suspension of TiO₂ and risk assessment of its degradation products, *Environ. Sci. Technol.* 47 (2013) 2704–2712.
- [65] T. An, H. Yang, W. Song, G. Li, H. Luo, W.J. Cooper, Mechanistic considerations for the advanced oxidation treatment of fluoroquinolone pharmaceutical compounds using TiO₂ heterogeneous catalysis, *J. Phys. Chem. A* 114 (2010) 2569–2575.
- [66] H. Yang, G. Li, T. An, Y. Gao, J. Fu, Photocatalytic degradation kinetics and mechanism of environmental pharmaceuticals in aqueous suspension of TiO₂: a case of sulfa drugs, *Catal. Today* 153 (2010) 200–207.
- [67] X. Hu, X. Hu, Q. Peng, L. Zhou, X. Tan, L. Jiang, C. Tang, H. Wang, S. Liu, Y. Wang, Mechanisms underlying the photocatalytic degradation pathway of ciprofloxacin with heterogeneous TiO₂, *Chem. Eng. J.* 380 (2020), 122366.
- [68] Y. Hai, A. Taicheng, L. Guiying, S. Weihua, W.J. Cooper, L. Haiying, G. Xindong, Photocatalytic degradation kinetics and mechanism of environmental pharmaceuticals in aqueous suspension of TiO₂: a case of β -blockers, *J. Hazard. Mater.* 179 (2010).
- [69] T. An, H. Yang, G. Li, W. Song, W.J. Cooper, X. Nie, Kinetics and mechanism of advanced oxidation processes (AOPs) in degradation of ciprofloxacin in water, *Appl. Catal. B Environ.* 94 (2010) 288–294.